Analysis of ducted fuel injection at high-pressure transcritical conditions using large-eddy simulations

Jack Guo[1] , Davy Brouzet[1], Wai Tong Chung[1] and Matthias Ihme[1,2]

Abstract

Ducted fuel injection (DFI) is a proposed fuel injection concept for achieving substantial reductions in emissions. In this concept, the fuel is injected through a coannular duct, resulting in increased fuel-air mixing and minimized formation of soot and other unwanted combustion products. Apart from comprehensive experimental investigations on DFI, so far computational studies have been limited to single-point Reynolds-averaged Navier Stokes simulations. Therefore, the objective of this work is to complement these studies by performing large-eddy simulations using a diffuse-interface method to examine the physical mechanisms and combustion processes of DFI, specifically focusing on the mixing process and the effect of fuel-ducting on combustion and pollutant emissions. To this end, finite-rate chemistry simulations are performed of the DFI configuration corresponding to the Engine Combustion Network Spray A injector at transcritical conditions (n-dodecane fuel, 60 bar pressure and 1000 K temperature chamber conditions). A two-equation soot model is employed for the qualitative analysis of soot emissions. Direct comparisons of averaged and instantaneous flow field results with the Spray A configuration are performed to assess the effect of DFI on the first- and second-stage ignition and soot formation. Compared to the free-spray condition, the results show that the DFI case exhibits a combination of (i) increased mass flow rate and entrained air, (ii) larger pressure drop magnitude and flow velocity, and (iii) a closer-to-stoichiometric mixture composition (both globally and locally), each of which is conjectured to contribute toward reduced soot production.

Keywords

Diesel engine, ducted fuel injection, supercritical fluid, diffuse-interface method, finite-rate chemistry, large-eddy simulations, Engine Combustion Network

Introduction

Diesel engines offer higher efficiency than spark ignition engines and are widely used as heavy-duty engines in the transportation sector.[1] However, diesel engines are prone to generate harmful emissions such as soot and nitrogen oxides (NO$_x$). As such, numerous strategies have been investigated to mitigate the formation of these harmful substances.[2,3] One proposed solution for decreasing soot formation as well as increasing engine efficiency involves the employment of the so-called ducted fuel injection (DFI), which was first proposed experimentally by Mueller et al.[4] In this DFI setup, a liquid fuel is injected as a spray at high-pressure conditions through a coannular duct. The ducted confinement modifies the dynamics and structure of the fuel spray and reduces the soot produced when compared to a standard non-ducted free spray.

DFI is only one of numerous combustion strategies examined to reduce engine emissions. Other strategies are after-treatment systems, such as diesel particulate filters and catalytic systems.[5,6] While after-treatment systems have demonstrated success in reducing emissions, they are also generally expensive, require regular maintenance and

[1]Department of Mechanical Engineering, Stanford University, Stanford, CA, USA
[2]Department of Photon Science, SLAC National Accelerator Laboratory, Menlo Park, CA, USA

Corresponding author:
Matthias Ihme, Department of Mechanical Engineering, Stanford University, 488 Escondido Mall, Building 530, Stanford, CA 94305, USA.
Email: mihme@stanford.edu

monitoring, and can require additional fluids for their operation. After-treatment systems also generally involve decreases in fuel efficiency. Other emissions reduction technologies include the development of low-sooting fuels such as oxygenated fuels [3,7]; these new fuels are often combined with variations in injector-tip configurations.[8] These approaches generally suffer from drawbacks such as high fuel costs, commercial unavailability of certain fuels, ineffectiveness at heavier engine-load conditions, and decreased fuel efficiency. Compared to these other techniques, DFI exhibits advantages in simplicity, low cost, ease of installation, lack of extensive maintenance needs, and general usability regardless of engine operating conditions or fuel. These positive aspects all make DFI an attractive approach to investigate as a more widely used emissions-reduction technology.

Mixing is a key hypothesized behavior in explaining the physical behavior of DFI, as discussed by Mueller et al.[4] The presence of the duct walls confines the liquid fuel spray, which increases the axial component of spray velocity while limiting overmixing at the radial periphery. The solid duct walls themselves also are hypothesized to increase mixing, both hydrodynamically and thermally.[4] The inner wall of the duct enforces a no-slip boundary condition on the fluid, resulting in steeper velocity gradients, which are not present in an unconfined free spray. The associated increase in the shear rate is thus thought to increase the turbulence and scalar mixing. Furthermore, variation in temperature between the duct and the interior fluid is hypothesized to increase the thermal mixing.

A number of studies have discussed the resultant effect of mixing on the velocity, temperature, and chemistry fields of the spray.[9–12] These studies broadly agree that the DFI spray – when compared with an unconfined free spray – is faster and cooler at the duct exit; as the spray continues downstream of the duct, these features promote increased fuel-air mixing. With this increased mixing comes a longer ignition delay time and larger lift-off length, resulting in more complete combustion and decreased soot production. However, a lack of consensus and understanding is present for certain aspects of the physics present. Specifically, Fitzgerald et al.[9] concluded that mixing enhancement happens only downstream of the duct exit and not within the duct, thus leading to a richer fuel-air mixture at the duct exit. Other studies[10,12] disagree and present results that show a leaner mixture at the duct exit. Additionally, the interaction between turbulence and the mixing is not fully understood. Such analysis requires scale-resolving turbulent calculations, and so performing such computations is a main objective of this work.

In addition to mixing, another important and related physical behavior for DFI is the entrainment of charge gas into the fuel spray, which has been investigated in different studies. Studies by Millo et al.,[13] Nilsen et al.,[14] and Zhang et al.[11] have shown enhanced levels of entrainment at the duct inlet compared to an unconfined free spray, which is attributed to the higher axial velocities and associated lower pressure within the duct interior. The low-pressure region within the duct then draws in fluid at the inlet to drive the increased entrainment; the phenomenon has been termed as a "jet-pump" effect. In contrast, Ong et al.[12] has found no evidence of enhanced inlet entrainment, and correspondingly no evidence of a region of significantly decreased pressure in the duct interior. In the context of this literature, one goal of our study is to investigate the existence of the inner-duct low-pressure region and whether enhanced entrainment occurs. These findings will be discussed in the Results section.

Previous studies in the literature have noted that entrainment of combustion products into the unconfined free spray appears to limit the success in soot attenuation.[8] Thus, within the duct, the wall is also hypothesized to provide a secondary effect of limiting the entrainment of combustion products into the spray; this "shielding" increases the lift-off length and helps contribute toward reduced soot formation.[4] At the outlet region between the duct and the lift-off length, increased entrainment is also hypothesized due to the longer lift-off length and longer ignition delay time observed for DFI.

Since the initial conception, DFI has been studied both experimentally and computationally. Experimental DFI studies by Gehmlich et al.[15] and Nilsen et al.[16] found significant soot reduction for a wide range of duct design parameters. Results showed that DFI was robust to parameters including duct length, axial gap between injector and duct inlet, ambient oxidizer mole fraction, and amount of dilution. For the purposes of comparing with and complementing experimental findings, computational studies of DFI have been carried out, especially in recent years. RANS studies at inert (non-evaporating and non-reacting) conditions have been performed by Zhang et al.[11] and Nilsen et al.[14] From these studies, the available information on averaged-flow quantities provided insight into the mixing and entrainment. RANS DFI studies at reacting conditions have also been performed[9,10,13] to gain insight into the interaction between the hydrodynamics and the reacting chemistry. Results from these studies complement experimental findings; the presence of the duct increases the ignition delay time and flame lift-off length, leading to increased mixing at the duct exit and resulting in attenuated soot.

Findings from these experiments and RANS studies have led to foundational understanding of the DFI physics. However, the need for higher-fidelity scale-resolving simulations has been recognized to more accurately capture the transient evolution of the physical processes present in spray combustion.[17] For this purpose, large-eddy simulations (LES) can provide detailed insights into the differences between DFI and unconfined free sprays. Ong et al.[12] performed LES incorporating a Lagrangian particle method to examine the effects of heat transfer from the duct in a DFI configuration. Good agreement with experimental data has

been reported with the use of such Eulerian-Lagrangian methods. However, these methods model the spray as a multiphase flow, which necessitates the selection of parameters for modeling breakup and evaporation and thus leads to parameter dependencies.

An alternative simulation method that can be employed in high-pressure flows, such as those encountered in diesel engines, is the diffuse-interface method.[18] Under trans- and supercritical conditions, the transitions between liquid and gaseous phases are no longer distinguishable. This absence of a physical interface makes it attractive to thermodynamically represent the flow as a single phase using a real-fluid equation-of-state. This diffuse-interface method for fluids at supercritical pressures has been applied to LES studies[19–21] for Engine Combustion Network (ECN)[22] diesel configurations Spray A and Spray D.

The objective of this study is to perform LES to investigate DFI for n-dodecane injection at realistic engine-like thermodynamic conditions. We specifically focus to complement the existing understanding of DFI by providing insight from scale-resolving LES computations into the fluid and chemical behavior, including key differences from a free spray configuration (Spray A) that is operated at the same conditions. We consider both inert and reacting conditions. Our calculations involve a compressible Navier-Stokes formulation with realistic thermodynamic considerations to represent the thermodynamic behavior of fluids at supercritical states. In Section 2 (Methods and computational setup), the mathematical model and computational configuration are presented. The results and their associated analyses are discussed in Section 3 (Results), and the paper finishes with conclusions in Section 4 (Conclusions).

Methods and computational setup

Governing equations

In the present study, we solve the conservation equations for Favre-filtered mass, momentum, total energy, and chemical species:

$$\partial_t \bar{\rho} + \nabla \cdot (\bar{\rho}\tilde{u}) = 0 \tag{1a}$$

$$\partial_t(\bar{\rho}\tilde{u}) + \nabla \cdot (\bar{\rho}\tilde{u}\tilde{u}) = -\nabla \cdot (\bar{p}I) + \nabla \cdot (\overline{\tau_v} + \overline{\tau_{SGS}}) \tag{1b}$$

$$\partial_t(\bar{\rho}\tilde{e}_t) + \nabla \cdot [\tilde{u}(\bar{\rho}\tilde{e}_t + \bar{p})] = \nabla \cdot [(\overline{\tau_v} + \overline{\tau_{SGS}}) \cdot \tilde{u}] - \nabla \cdot (\overline{q_v} + \overline{q_{SGS}}) \tag{1c}$$

$$\partial_t(\bar{\rho}\tilde{Y}_k) + \nabla \cdot (\bar{\rho}\tilde{u}\tilde{Y}_k) = -\nabla \cdot (\overline{J_{k,v}} + \overline{J_{k,SGS}}) + \overline{\dot{\omega}_k} \tag{1d}$$

where ρ is the density, u is the velocity vector, p is the pressure, e_t is the specific total energy, τ is the stress tensor, and q is the heat flux. Y_k, J_k and $\dot{\omega}_k$ are the mass fraction, diffusion flux, and chemical source term for species k, respectively. The overline denotes traditional LES filtering, and the tilde denotes Favre-

filtering; for a quantity ϕ, $\tilde{\phi} = \overline{\rho\phi}/\bar{\rho}$. For τ and q, Chung et al.'s method with high-pressure correction[23] is used to evaluate the dynamic viscosity μ and the thermal conductivity λ. For binary diffusion coefficients, Takahashi's high-pressure correction[24] is employed. The subscript v is used for viscous quantities, and the subscript SGS denotes subgrid-scale turbulent quantities. We employ the Peng-Robinson (PR) equation of state[25] (EoS):

$$p = \frac{\rho RT}{1 - b\rho} - \frac{\rho^2 a}{1 + 2a\rho - b^2\rho^2}, \tag{2}$$

to close the governing equations. Here, R is the mixture-specific gas constant, T is the temperature and the coefficients a and b depend on mixture composition and temperature.[26] The PR EoS has been shown to perform well in describing fluid thermodynamics at transcritical conditions.[27–29] Details for evaluating necessary thermodynamic quantities for mixtures are provided in Ma et al.[30]

The reaction chemistry in this numerical study is modeled using a reduced 33-species chemical mechanism,[19] and 21 additional species have been identified as suitably modeled using a quasi-steady-state assumption. The soot dynamics of the system are modeled using the Moss-Brookes model,[31] which has been used in previous diesel and n-dodecane injection studies[32,33] as well as specifically in DFI studies.[12] This model consists of a set of two coupled partial differential equations (PDEs), written as:

$$\frac{\partial(\rho Y_{soot})}{\partial t} + \nabla \cdot (\rho u Y_{soot}) = \nabla \cdot (D_{soot}\nabla Y_{soot}) + \dot{M} \tag{3a}$$

$$\frac{\partial(N/N_A)}{\partial t} + \nabla \cdot \left(\frac{uN}{N_A}\right) = \nabla \cdot \left(D_{soot}\nabla\left(\frac{N}{\rho N_A}\right)\right) + \dot{N} \tag{3b}$$

where Y_{soot} is the soot mass fraction, D_{soot} is the soot diffusivity (given using an eddy viscosity/Schmidt number approximation), N is the soot number density and N_A is Avogadro's constant. $\dot{M}$ and $\dot{N}$ are the soot mass and soot number density source terms, respectively, and are given as

$$\dot{M} = \frac{M_P}{N_A}\left[\left(\frac{dN}{dt}\right)_{inception}\right] + \left(\frac{dM}{dt}\right)_{surface\ growth} + \left(\frac{dM}{dt}\right)_{oxidation} \tag{3c}$$

$$\dot{N} = \frac{1}{N_A}\left[\left(\frac{dN}{dt}\right)_{inception} + \left(\frac{dN}{dt}\right)_{coagulation}\right] \tag{3d}$$

where M_P is the mass of an incipient soot particle; a value of $M_P = 144$ kg/kmol, is used, corresponding to the mass of particles comprising 12 carbon atoms. The model performance is not sensitive to the value of M_P.

Expressions for the semi-empirical source and sink terms provided in equation (3c) and (3d) follow the formulation provided in Watanabe et al.[34] and are given as

$$\left(\frac{dN}{dt}\right)_{inception} = C_\alpha N_A \left(\frac{\rho Y_{C_2H_2}}{MW_{C_2H_2}}\right) \exp\left(-\frac{T_\alpha}{T}\right) \quad (3e)$$

$$\left(\frac{dN}{dt}\right)_{coagulation} = -\left(\frac{24\hat{R}}{\rho_s N_A}\right)^{0.5} \left(6\frac{\pi}{\rho_s}\right)^{\frac{1}{6}} T^{\frac{1}{2}} (\rho Y_s)^{\frac{1}{6}} N^{\frac{11}{6}}$$
$$(3f)$$

$$\left(\frac{dM}{dt}\right)_{surface\ growth} = C_\gamma \left(\frac{\rho Y_{C_2H_2}}{MW_{C_2H_2}}\right)$$
$$\exp\left(-\frac{T_\gamma}{T}\right) \left[(\pi N)^{\frac{1}{3}} \left(6\frac{\rho Y_s}{\rho_s}\right)\right]^{\frac{2}{3}}$$
$$(3g)$$

$$\left(\frac{dM}{dt}\right)_{oxidation} = C_{oxid,OH} \left(\frac{\rho Y_{OH}}{MW_{OH}}\right) \eta_{coll} T^{\frac{1}{2}}$$
$$\left[(\pi N)^{\frac{1}{3}} \left(6\frac{\rho Y_s}{\rho_s}\right)\right]^{\frac{2}{3}} + C_{oxid,O_2} \left(\frac{\rho Y_{O_2}}{MW_{O_2}}\right) T^{\frac{1}{2}} \left[(\pi N)^{\frac{1}{3}} \left(6\frac{\rho Y_s}{\rho_s}\right)\right]^{\frac{2}{3}}$$
$$(3h)$$

where $\hat{R}$ is the universal gas constant, MW_i refers to the molecular weight of species i, ρ_s refers to the soot density $= 1800\ kg/m^3$, and all other variables C_i, T_i, and η_i are empirical constants defined in Watanabe et al.[34]

Numerical solver

The numerical simulations are computed using a compressible unstructured finite-volume solver. A sensor-based hybrid scheme[35] is used to discretize the convective fluxes, with an added entropy-stable flux correction technique developed by Ma et al.[18] A second-order Strang-splitting scheme[36] is used to separate the convection, diffusion, and reaction operators. The chemical source terms are time-integrated using a semi-implicit fourth-order Rosenbrock-Krylov (ROK4E) scheme,[37] which has linear cost with respect to the number of species. All other operators are integrated using a strong stability-preserving third-order Runge-Kutta (SSP-RK3) scheme.[38] The Vreman SGS model[39] is used to model the sub-grid turbulent stresses. A dynamic thickened-flame model[40] is utilized, with maximum thickening factor set to a value of 4.

Computational setup

The thermodynamic conditions of the numerical studies we perform follow those of the ECN Spray A configuration, which has been used as a standardized design for compression injection engine sprays in a wide variety of studies and applications.[41] Our study focuses primarily on the reacting conditions, but inert conditions are also considered to examine features of the hydrodynamics. For inert and reacting settings, the ambient pressure is

$p_\infty = 6.00\ MPa$, the duct temperature is $T_{duct} = 461\ K$, and the injection pressure is $p_{rail} = 150.0\ MPa$. The inert cases have ambient temperature $T_\infty = 900\ K$ and ambient oxygen mole fraction of 0.0%, while the reacting conditions have $T_\infty = 1000\ K$ and ambient oxygen mole fraction of 21.0%.

The results and discussion by Ong et al.[12] emphasize the importance of the DFI results (specifically the ignition delay time and the flame lift-off length) on the so-called "dwell period." The dwell period is defined as the time period between the initial preburn spark ignition and the start of fuel injection in an experimental combustion chamber setup. Following this guideline by Ong et al.[12] our study uses the dwelled temperature field (found at the end of the dwell period) as the appropriate initial condition of the DFI simulation, meant to model the effects of the experimental spark ignition and dwell period. To arrive at the dwelled temperature field, the initial temperature of the fluid phase within the duct is prescribed by the solution to the steady-state heat equation. For the boundary conditions of this steady-state heat equation, the temperature at the inner diameter of the duct is set to be $T = T_{duct}$, and the temperature at the two lateral faces of the cylinder (at $x = 2\ mm$ and at $x = 16\ mm$) are set to be the ambient temperature $T = T_\infty$. Subject to these boundary conditions, the temperature field then evolves to reach the steady-state solution, which we use as the starting point of the LES.

Our present study uses the D3L14G2 duct configuration, following the specification and naming convention introduced by Mueller et al.[4] This setup involves a duct with inner diameter of 3 mm, wall thickness of 1 mm, cylinder axial length L of 14 mm, and an offset (or "stand-off distance") G of 2 mm of the duct inlet from the fuel injector location. A 45° × 0.5 mm chamfer is applied to the inner diameter at the inlet and outlet of the duct.

The computational domain is a three-dimensional cylinder, discretized by a structured mesh with 2.20 million hexahedral elements. The domain dimensions are 40 mm in diameter and 100 mm in axial length. The mesh is adapted from the one used in Chung et al.[21] with the duct geometry added in as an additional element. A minimum grid spacing of 8 μm in the spray core is chosen to resolve the ignition kernels. The domain and mesh are shown in Figure 1. Numerous previous studies have observed and discussed the significant variability in spray behavior and engine metrics due to variations in the nozzle internal geometry, whether from intentional design choices, manufacturing inconsistencies, or unintentional discrepancies in operation conditions.[42,43] To remove this potential source of uncertainty, the injector geometry is not included in the simulations. Instead, inlet boundary conditions to match nozzle conditions as prescribed by ECN[44] are assigned. The injector model is serial #210675, which has a nozzle outlet diameter of 89.4 μm. The inlet fuel mass flux is determined with a time-dependent rate of
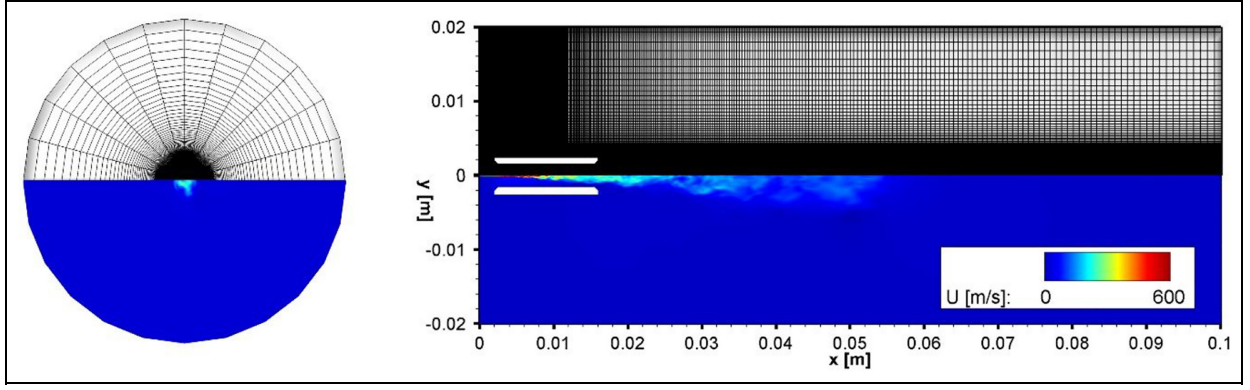
Figure 1. Radial (left) and axial (right) view of mesh used, along with velocity magnitude profiles. The duct is visible in the axial view. The mesh consists of 2.20 million grid points. Minimum cell size is 8 μm.
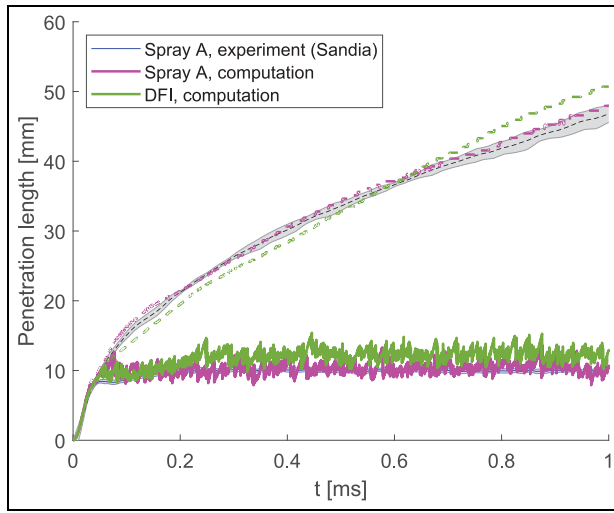

Figure 2. Comparison of liquid (solid line) and vapor (dashed line) penetration lengths for the inert DFI case. Experimental comparisons for the free spray are also provided. The gray envelope around the experimental profiles represents the standard deviation around the mean value.

injection, as provided by the CMT virtual injection rate generator.[45] The solution is advanced with a unity CFL number for time-stepping, resulting in a typical time step of 5×10^{-9} s.

Results

Engine performance quantities: Inert cases

Figure 2 compares the penetration lengths of the inert simulations for both the DFI case and the free spray case, with standard conditions of $p_\infty = 6.00\ MPa$ and $T_\infty = 900K$ as specified by ECN. The results for the Spray A case corresponds to data presented in Chung et al. [21]; experimental data is from Lillo et al.[44] and Westlye et al.[46] using Schlieren imaging for vapor penetration length and Mie scattering for the liquid penetration length. The vapor penetration length is defined as the furthest axial position where the mixture fraction Z_B

exceeds 0.01, and the liquid penetration length uses a value of $Z_B = 0.6$, following Bilger's definition for Z_B.[47]

The vapor penetration length for the DFI case does not show significant deviation from that of free spray computations or experiments; this observation is consistent with findings by Ong et al.[12] and Li et al. [48] Ong et al.[12] also observed significant increase in the DFI liquid penetration length (an increase in excess of 50%, with a peak value occurring at around 0.4 *ms*) that then decreases down to the free spray value at later times. In our current study, we note that the liquid penetration length is larger in the DFI case by 25% when compared to the free spray case. This enlargement in the DFI case can be explained by the presence of cooler, higher-density fluid inside the duct, which is a feature of the dwelled temperature field due to the effects of the spark ignition and dwell period. This region of low temperature fluid attenuates the vaporization of the liquid fuel as the spray passes through the duct, thus contributing to the observed increase in liquid penetration length. From these observations, with respect to the inert mixing of species, the DFI and free spray cases exhibit subtle differences that arise from the presence of the duct. Many modern compression-ignition engines operate at pressures larger than investigated in the current study. At such increased pressures, studies have found that the increased ambient gas density leads to stronger spray drag and thus a decreased liquid penetration and a slower vapor penetration.[49]

Engine performance quantities: Reacting cases

To illustrate the differences in the dynamic evolution of the reacting spray for the DFI and free spray cases, Figure 3 shows contour plots at a centerline plane for temperature and mass fractions of intermediate species: OH mass fraction contours as an indication of high temperature chemistry, and CH_2O mass fraction contours as an indication of low temperature chemistry. Snapshots are given at various times offset the ignition delay time (τ_{ign}). From the temperature fields, the effects of DFI in modifying the structure of the spray and flame, including
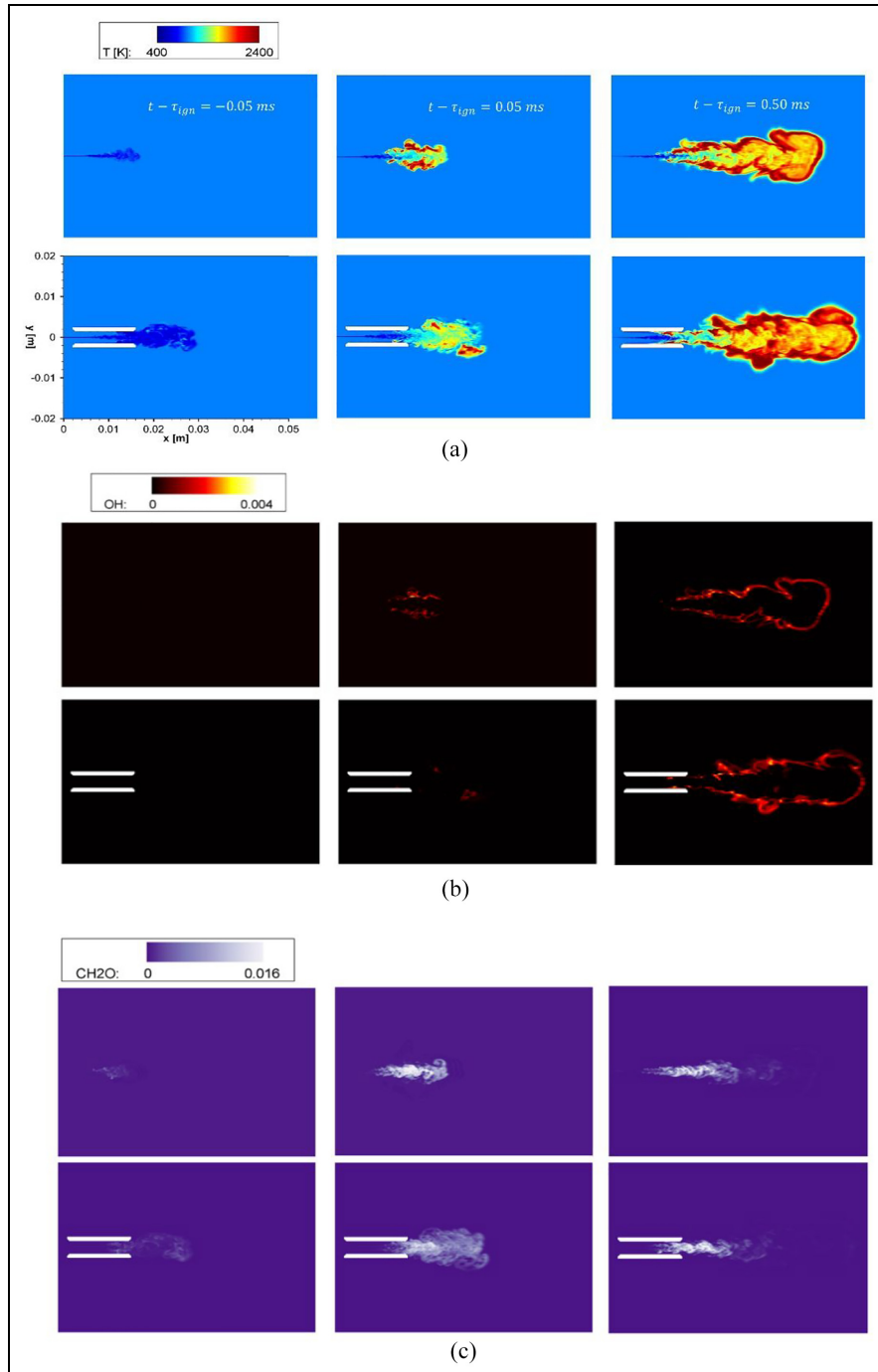
Figure 3. Instantaneous flow-field results for (a) temperature, (b) Y_{OH}, and (c) Y_{CH_2O} for the free spray case (top) and the DFI case (bottom) at various times offset by the ignition delay time, $t - \tau_{ign}$; from left to right, $t - \tau_{ign} = -0.05$ *ms*, 0.05 *ms* and 0.5 *ms*. $\tau_{ign} = 0.145$ *ms* in the free spray case, and $\tau_{ign} = 0.447$ *ms* in the DFI case.

in lengthening the flame lift-off position with respect to the injector location, are visible. Starting from the first snapshot just before ignition at $t - \tau_{ign} = -0.05$ *ms*, formation of CH_2O is observable in the core region in both cases, although in the DFI case the contour values far downstream of the duct exit are more diffuse in volume, indicating the presence of increased mixing. In the free spray at later times, an increased presence of OH coincides with the consumption of CH_2O near the spray periphery as noted in Chung et al.[21] For the DFI,

the consumption of CH_2O at the spray edges is more pronounced compared to the free spray case, despite there still being an increase of OH at later times for both cases. To complement this discussion of the temperature and the important chemical species, details regarding the differences in axial velocity and pressure between the DFI and free spray cases will be discussed in Section 3.3 (Flow Analysis).

To provide insight into the ignition behavior and to examine the lift-off length, Figure 4 compares planar-
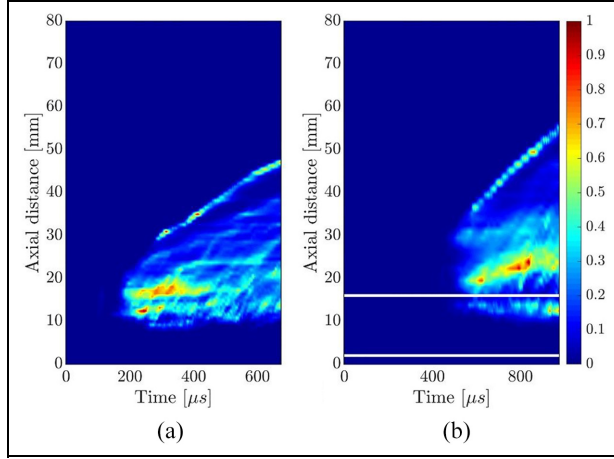
Figure 4. Planar-integrated OH intensity $I_{xt,OH}$ for (a) the free spray case and (b) the DFI case. The results are normalized to be 0 at the minimum intensity and 1 at the maximum intensity. The duct inlet ($x = 2$mm) and outlet ($x = 16$mm) locations are provided in the DFI case as white lines.

Figure 5. Computed values of ignition delay time τ_{ign}, for the DFI case (red) and the free spray case (blue). Values from literature are given as comparison Note that the data by Mueller et al.[4] has been corrected by a reported hydraulic delay of 0.32 ms.

Table 1. Comparison of flame lift-off length from literature and current investigation.

Case	DFI lift-off length (mm)	Free Spray lift-off length (mm)
Gehmlich et al.[15]	14.73	8.41
Mueller et al.[4]	16.68	10.00
Present investigation	12.26	8.15

integrated intensity plots of OH for the free-spray case (left) and the DFI case (right). The intensity $I_{xt,OH}$ is given as [50]:

$$I_{xt,OH}(x,t) = \int \tilde{Y}_{OH}(x,y,t)dy \qquad (4)$$

From Figure 4, the delayed ignition delay time for the DFI case is clearly visible. Regions of high OH (indicative of high-temperature chemistry) occur further downstream for the DFI case as also seen in visualizations of the temperature and species contours in Figure 3. The flame lift-off length is visualized by the region of the luminous zone closest to the ignition point in Figure 4. In Table 1, the lift-off lengths for both experimental measurements and for our results are listed. Following ECN recommendations, the lift-off length is defined as the minimal axial distance from the injection location to the point where 2% of the maximal OH mass fraction is found.

For both the DFI and the free spray case, the lift-off length is underpredicted with respect to experimental values. The differences in computational and experimental methodologies for calculating the lift-off length likely accounts for some of this discrepancy. Experimentally, the lift-off length is computed using the axial location at which a threshold of pixel intensity is used to capture the OH* chemiluminescence.
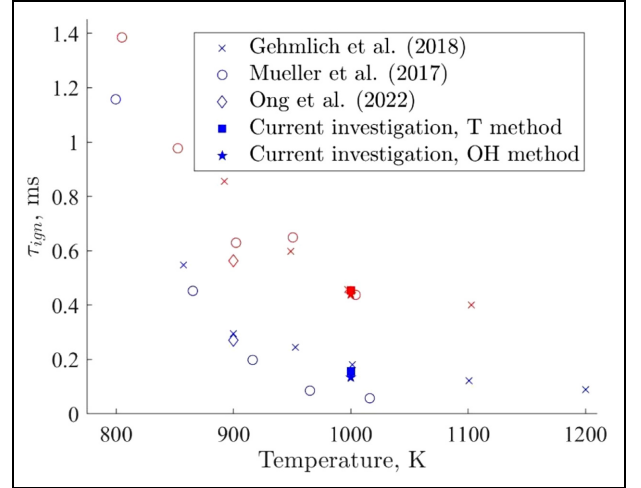
Quantifying the error produced by these different methodologies has not been well-reported and would require further investigation. Other sources of discrepancy include potential experimental duct misalignment[4] and limited experimental optical access for lift-off length values within the duct. Overall, the amount of deviation from experimental values is comparable to that found in the computational study by Ong et al.[12] and is within the range of typical experimental uncertainty.[51] Even with these experimental/computational discrepancies, the DFI's effect in increasing the lift-off length by approximately 50% with respect to the free spray case is captured, consistent with the percentage increase found in the experimental values at the same condition.

Figure 5 compares the ignition delay time predictions for both the DFI and free spray cases with experimental results by Mueller et al.[4] and Gehmlich et al.[15] The results of two different methodologies for calculating the ignition delay time are presented. The T-method is used by Ong et al.[12] and defines the ignition delay time to be the time at which the rate of change of the maximum temperature in the domain is the largest. The OH-method instead determines the time at which 14% of the maximum OH mass fraction is reached; this method has been found to be in good agreement with experimental measurements based on a 50% OH* chemiluminescence.[52] For our cases, both methods yield similar results, with $< 14\%$ and $< 4\%$ discrepancy for the free spray case and for the DFI case, respectively. Both methods also produce quantitative agreement with experimental results.

Just as we did when discussing the inert penetration behavior, we again make note that ambient pressures larger the current study's 6.00 MPa are found in many modern compression-ignition engines. At these increased
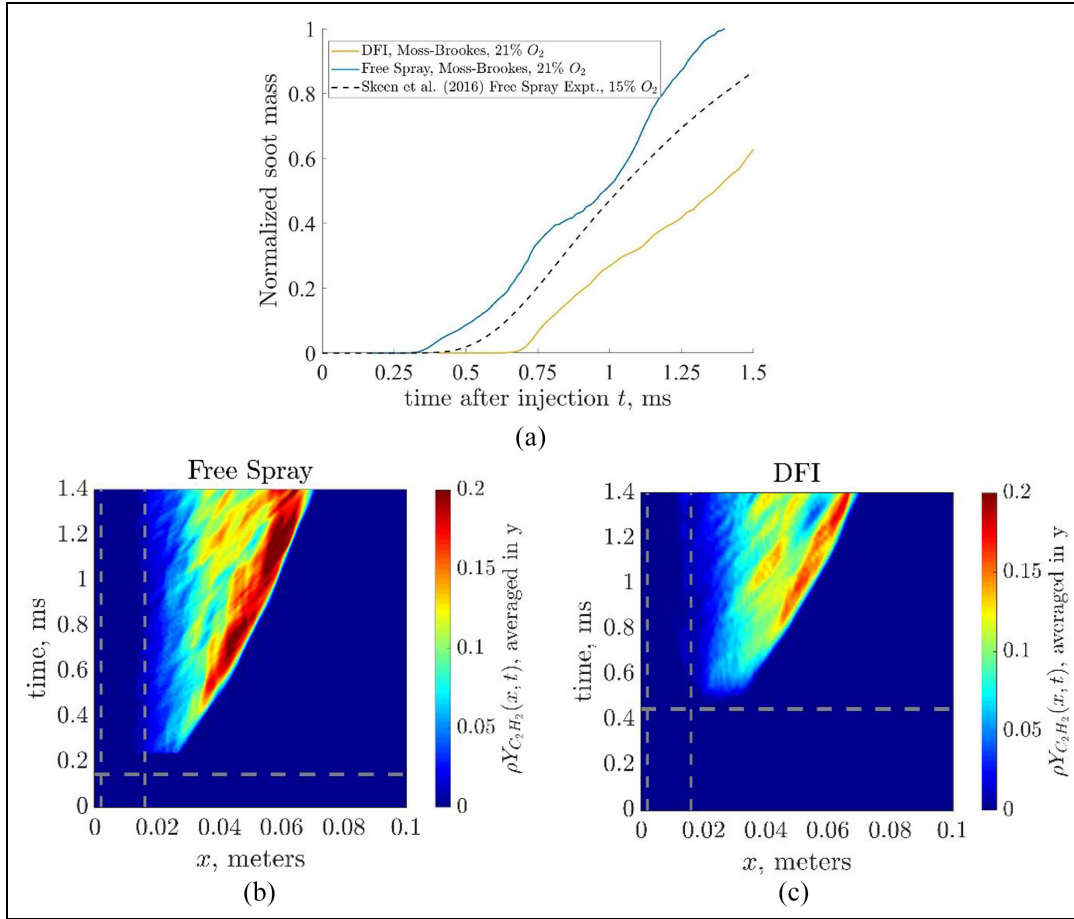
Figure 6. (a) Volume integrated total soot mass as provided by the Moss-Brookes soot model as a function of time after injection. DFI and free spray soot computational profiles are normalized by the maximum free spray value of 318.87 μg. Dotted lines shown a comparison profile of experimental measurements at the same 1000K ambient temperature but at a reduced ambient O_2 volume concentration of 15%, as provided by Skeen et al. [51]; maximum soot value for this experimental case is 48.34 μg. Bottom panels show the radially integrated planar $\rho Y_{C_2H_2}$ profiles in x and t for (b) free spray and (c) DFI. Vertical gray lines denote the duct edges (in which the duct is only physically present in the DFI case), while the horizontal gray line is drawn at the ignition delay time (τ_{ign}).
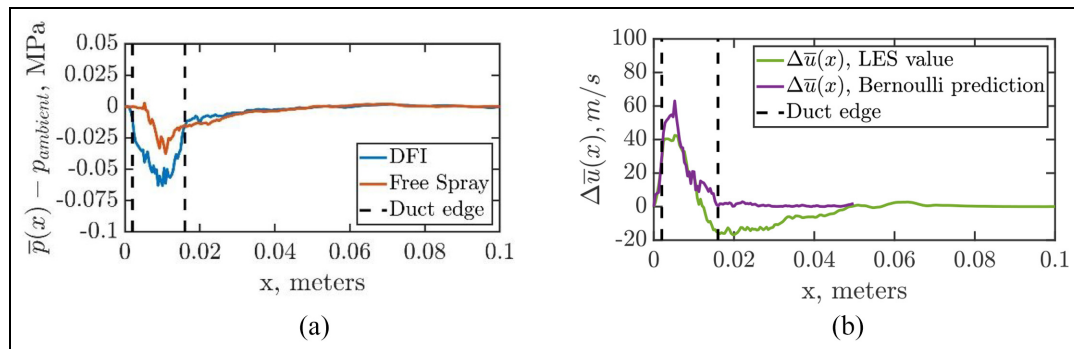

Figure 7. (a) Time- and planar-averaged pressure $\bar{p}(x)$ profiles as a function of axial distance from jet, and (b) LES value and Bernoulli prediction as per equation (7) of the streamwise velocity increase in the DFI case, $\Delta\bar{u} = \bar{u}_{DFI}(x) - \bar{u}_{FS}(x)$. In both cases, conditional averaging is performed for $|y| \leqslant r_{duct}$. Time averaging is performed for the interval $0 \leqslant t \leqslant 1.4$ ms. Vertical black lines denote the duct edges (in which the duct is only physically present for the DFI case).

pressures, studies have shown that reduced ignition delay time and shortened lift-off length are observed.[53]

Figure 6 shows profiles of soot mass and contours of C_2H_2 as soot precursor. From the integrated soot mass profiles shown in Figure 6(a), we see that, at equivalent times, the soot mass in the DFI case is attenuated compared to the free spray case, and the rate of soot production is also lower in the DFI case; both
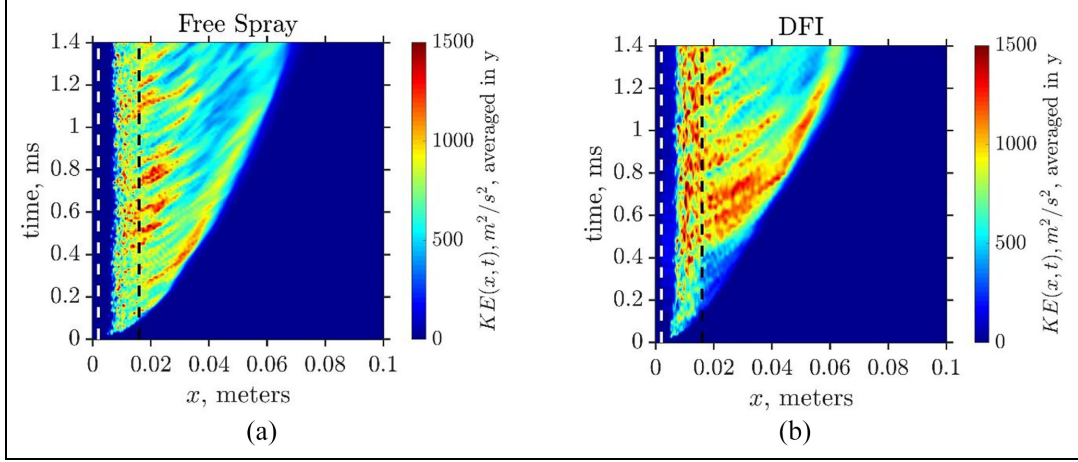
Figure 8. Planar-averaged kinetic energy profiles as a function of the streamwise distance and time for the (a) free spray case and (b) for the DFI case. The dashed line (white for the inlet edge, black for the outlet edge) denotes the location of the inlet and outlet of the duct; note that the duct is only physically present in the DFI case.

observations are consistent with experimental findings.[4,15] Comparison of normalized profiles between the current study's free spray case and the experimental case from Skeen et al.[51] yield qualitatively comparable behavior. Due to differences in the O_2 concentration, we note that certain differences (such as the earlier soot onset at higher oxygen concentrations) are expected, as found in previous studies.[15] From the time-evolving plots of spatial C_2H_2 provided in Figure 6(b) and (c), we can observe that the DFI case displays a delayed and decreased amount of C_2H_2, with peak values occurring further downstream of the injection site.

Flow analysis

From Figure 7(a), we observe a significant influence of the duct on the hydrodynamic pressure, with the mean pressure deviation in the DFI case being approximately twice less than the free spray value within the duct. At its minimum, the DFI $\bar{p}(x)$ is 1.05% less than the quiescent ambient pressure of 6.0 MPa, while the free spray $\bar{p}(x)$ reaches a minimum of 0.63% less than the ambient value.

This difference in $\bar{p}(x)$ results in an observable effect on the resultant flow dynamics, specifically in increasing the fluid velocity within the duct compared to the free spray. This can be mathematically estimated using the compressible Bernoulli equation with gravity neglected, which can be written as:

$$\frac{u_i u_i}{2} + \int_{p_1}^{p} \frac{d\bar{p}}{\rho} = const, \tag{5}$$

where p_1 is a reference pressure for which we use the ambient pressure value of 6.0 MPa. Assuming the fluid velocity magnitude is dominated by the streamwise component and considering a streamline from the ambient inlet in the far-field to a point with radius less than the duct inner radius, we arrive at

$$\left(\frac{\bar{u}^2}{2} + \int_{p_1}^{p} \frac{d\bar{p}}{\rho}\right)_{DFI} = \left(\frac{\bar{u}^2}{2} + \int_{p_1}^{p} \frac{d\bar{p}}{\rho}\right)_{FS}, \tag{6}$$

where the FS subscript denotes the quantities in the free spray case. We can now solve for the difference between the DFI and free spray velocities as

$$\bar{u}_{DFI} = \sqrt{\bar{u}_{FS}^2 - 2\left(\int_{p_1}^{\bar{p}} \frac{d\bar{p}}{\rho}\right)_{DFI} + 2\left(\int_{p_1}^{\bar{p}} \frac{d\bar{p}}{\rho}\right)_{FS}} \tag{7}$$

Comparisons of the LES values of the time-averaged streamwise velocity and the Bernoulli prediction per equation (7) are shown in Figure 7(b). Reasonable agreement in obtaining the magnitude and trend of the velocity increase $\Delta\bar{u} = \bar{u}_{DFI}(x) - \bar{u}_{FS}(x)$ is obtained inside the duct. Note that to use equation (7), a temporally-steady flow is required, and so we only expect reasonable results for the x-extent of the domain within the duct. This reasoning is supported by the planar radially-averaged kinetic energy contours in Figure 8, which show that although the overall flow field is temporally evolving as the vapor penetration grows, the behavior of the kinetic energy within the duct edges (or where the duct would be in the free spray case) reaches a steady-state behavior. Accordingly, as seen in Figure 9, the Bernoulli estimate is less accurate downstream of the duct exit, likely due to the unsteady nature of the vapor-like portion of the spray. From Figure 8(b), we also observe that the DFI in-duct kinetic energy is noticeably larger than the free spray value, thus confirming our observations in Figure 7, and potentially implying an increased turbulent mixing in the DFI case.

This Bernoulli analysis explains the contribution of the duct toward an increased turbulent flow rate, thus explaining the increased penetration (Figure 2) observed in the DFI case. In this context, we note that the jet-pump effect refers to the region of low-pressure
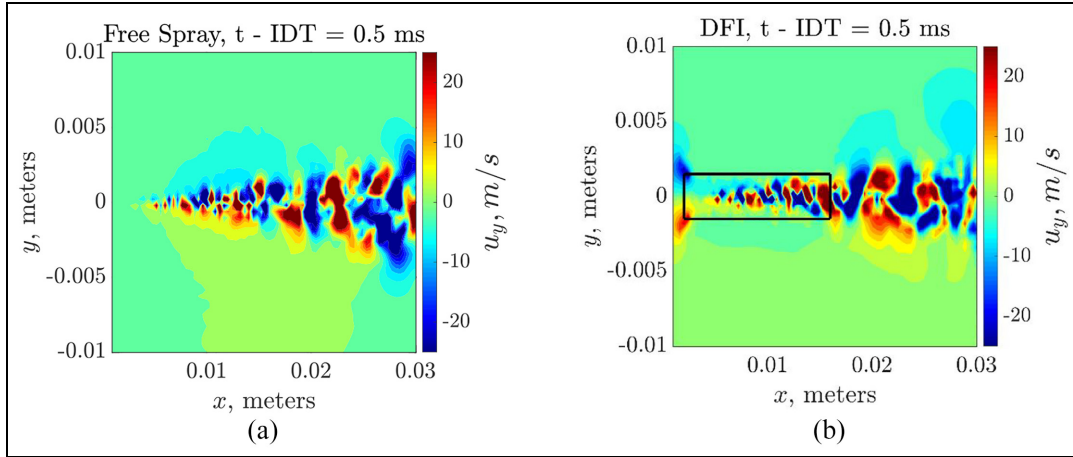
Figure 9. Centerline z-plane contours of instantaneous vertical velocity u_y for $t - t_{IDT} = 0.5$ *ms*, for the (a) free spray and (b) DFI cases. The black box in (b) denotes the duct location.
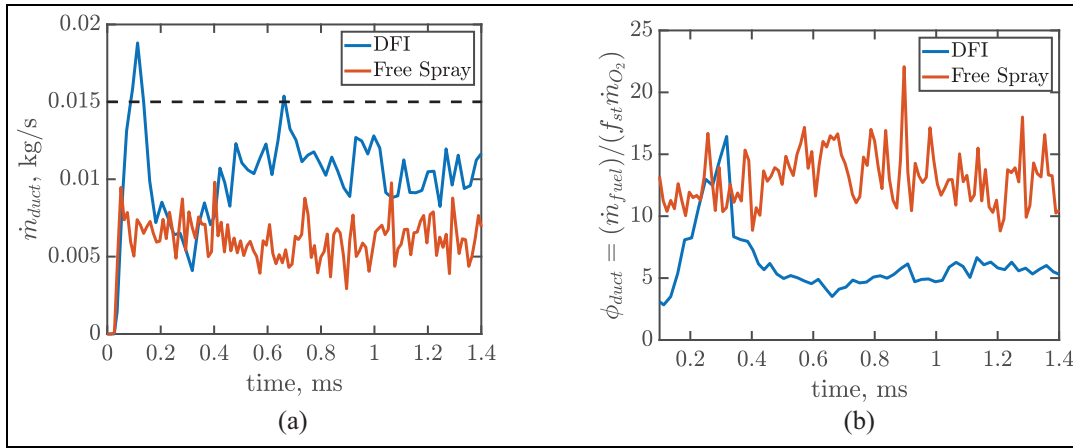

Figure 10. (a) Planar-integrated mass flow rates for $|y| \leqslant r_{duct}$, as a metric for the difference in entrainment between the free spray and DFI cases. The horizontal black dashed line shows the value estimated using equations (8) and (9). (b) Planar-integrated equivalence ratio for $|y| \leqslant$ duct inner radius, as a metric of the fuel-air composition, for both the free spray and DFI cases. The global equivalence ratio ϕ_{duct} is calculated as the ratio between the injection fuel mass flow rate and the O_2 mass flow rate, normalized by the stoichiometric fuel/O_2 ratio f_{st}. In both (a and b), the profiles are averaged for streamwise locations between $x = 7.5mm$ and $x = 10.5$ *mm*, as representative of in-duct locations.

created inside the duct, which has important consequences on the jet entrainment and fluid being drawn in at the duct inlet. The observations from our current investigation do indeed highlight a region of low pressure in the axial extent of the duct, which is accentuated in the DFI case. This finding provides further clarification to the conclusions discussed by Ong et al.[12] whose findings claimed no region of significant decrease in pressure and thus no jet-pump effect. Our results instead support the findings of previous RANS studies that showed evidence of the existence of a jet-pump effect that drives entrainment into the duct via a region of in-cylinder low pressure.[13,14]

It is evident from Figure 7 that the duct causes an enhancement of the streamwise flow velocity. While the previous analysis using Bernoulli's equation can be useful to estimate the added mass flow through the duct, it requires a priori knowledge of the pressure drop. The

duct and high velocity jet effectively work as an ejector. Using a simple momentum and energy balance, Pritchard et al.[54] have derived an analytical expression for the ratio between the mass flow of the primary and secondary jets, corresponding, respectively, to the fuel jet and entrained air flow in the present work. Their formulation can be expressed as

$$R_{\dot{m}} = \frac{\dot{m}_s}{\dot{m}_p} = \frac{-(1+\sigma)}{2\sigma} + \frac{D_{duct}}{D_p}\sqrt{\frac{1}{(1+C_L)\sigma}}, \qquad (8)$$

where the subscripts p and s denote the primary and secondary jets, respectively, $\sigma = \rho_p/\rho_s = 30.7$, and $D_{duct} = 3$ mm and $D_p = 0.09$ mm are the diameters of the duct and fuel injector, respectively. The skin friction coefficient C_L is set to a value of 0.3, following the computational work on ejectors of Singh et al.[55] Noting that the mass flow inside the duct is the sum of the
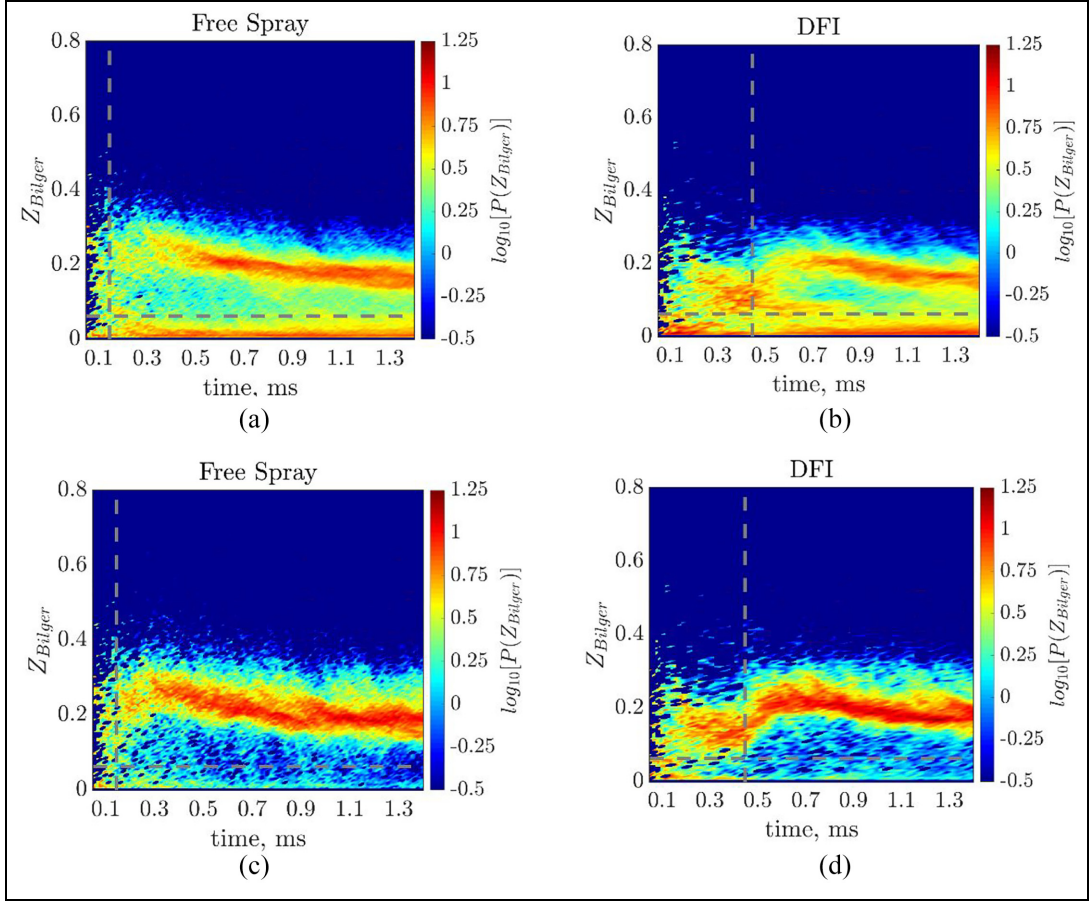
Figure 11. Plane-extracted probability distribution function (PDF) of Z_{Bilger} shown as a function of time. Vertical gray lines correspond to the ignition delay time (τ_{ign}) in each case, while the horizontal gray line provides the stoichiometric Z_{Bilger} value, $Z_{st} = 0.0628$. The logarithm, base 10, of PDF values are shown to aid in visualization. (a and b) show data for the entire domain, while (c and d) show data for $|y| \leqslant$ duct inner radius, to isolate the jet behavior from the ambient charge gas behavior.

primary and secondary mass flows, equation (8) can be rearranged as

$$\dot{m}_{duct} = \dot{m}_p(R_{\dot{m}} + 1), \tag{9}$$

In the present configuration, $R_{\dot{m}} = 4.75$ and $\dot{m}_{duct} = 15.0$ g/s which implies a large amount of air entrained in the duct. As postulated by previous investigators, this entrainment of ambient fluid into the duct is expected. This behavior is confirmed in the present configuration through Figure 9; in the region near the duct inlet, entrainment of fluid is visible in the DFI case through the inwards behavior of the vertical velocity. In the free spray, the shear caused by the jet introduces little entrainment, which is significantly lower than the one observed in the DFI case, according to Figure 9.

To perform a quantitative estimation of the difference in entrainment between the two cases, Figure 10(a) shows the total mass flow through the duct section (or a section of same size in the free spray case). The total mass flow in the DFI case is larger by approximately 80% due to the entrained air, once steady state is reached. The mass flow rate in the DFI case is 30%

lower than the analytical prediction from equations (8) and (9), which is depicted by the dashed line in Figure 10(a). The isentropic and ideal gas assumptions, necessary to derive the analytical formulation, might explain the discrepancy observed. It has also been noted in the literature that the axial location of the primary jet with respect to the duct inlet played a role in the level of mass flow entrained, potentially leading to a suboptimal entrainment.[55,56] Nevertheless, the analytical formulation seems to provide encouraging results as a tool to be further applied to DFI configurations.

The global equivalence ratio inside the duct, in Figure 10(b), shows the beneficial consequences of the entrainment on the mixing and subsequent combustion process. With a global in-duct mixture that is closer to stoichiometric, it can be expected that the resulting chemical reaction occurs closer to stoichiometric in the DFI case and thus leads to the soot decrease as seen in Figure 6.

To further analyze the effect of entrainment on the mixture composition, the transient mixing differences that arise from the presence of the duct in the DFI case are visualized using the PDF of Z_{Bilger}, shown as a
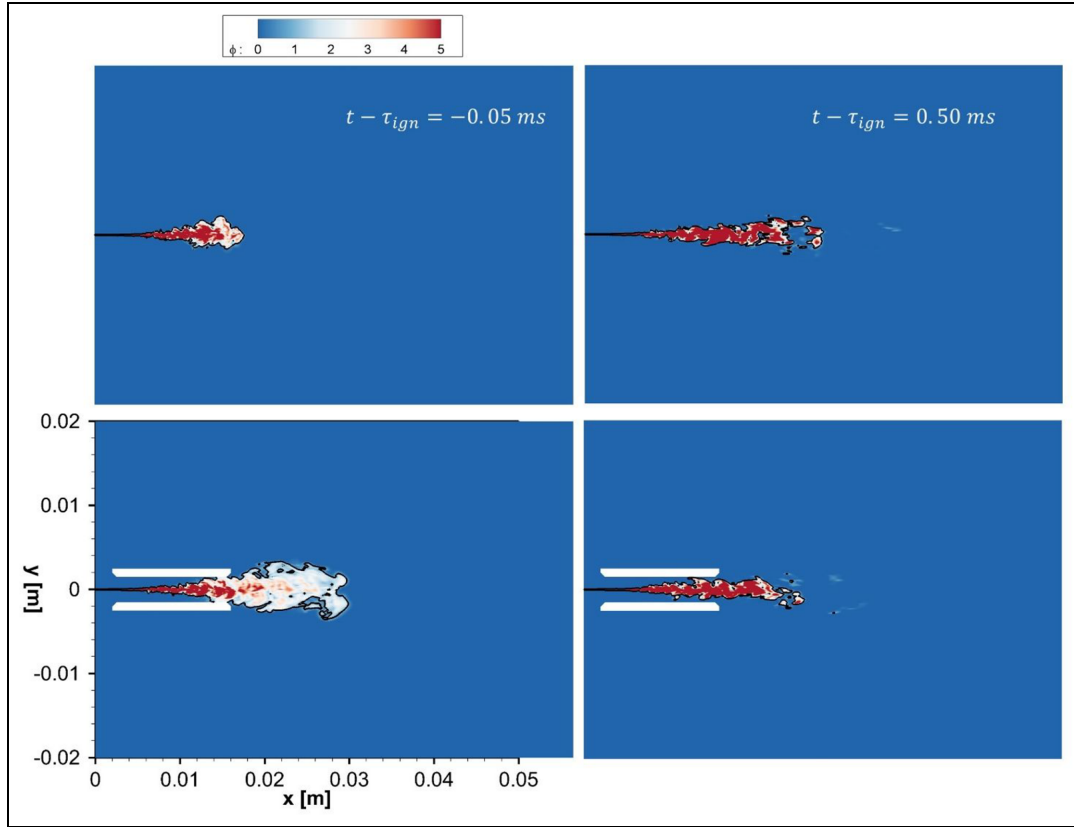
Figure 12. Contours of a) transient temperature local equivalence ratio, ϕ, for the free spray case (top) and DFI case (bottom) at various times offset by the ignition delay time, $t - \tau_{ign}$; from left to right, $t - \tau_{ign} = -0.05$ *ms* and 0.5 *ms*. $\tau_{ign} = 0.145$ *ms* in the free spray case, and $\tau_{ign} = 0.447$ *ms* in the DFI case. $\phi = 1$ is shown using a black contour line.

function of time in Figure 11. Of interest is the early mixing transient behavior, for $t \leqslant 0.5$ *ms*. Although ignition for the free spray case occurs at a relatively early time of 0.14 *ms*, the unsteady behavior of Z_{Bilger} in Figure 11 does suggest that significant mixing occurs up through (and after) 0.5 ms in both the DFI and free spray cases.

The zones of high probability in the free spray case are either too fuel-rich ($Z_{Bilger} > Z_{st}$) or too fuel-lean ($Z_{Bilger} < Z_{st}$) for optimal ignition. The fuel-lean side of the PDF distribution are relatively similar between the free spray and DFI case. However, the DFI case displays a region of high probability fuel-rich values closer to Z_{st} for 0.1 *ms* $\leqslant t \leqslant 0.5$ *ms*. This region of interest suggests improved mixing before and during ignition when the duct is present, with the closer-to-stoichiometric combustion producing decreased levels of incomplete combustion products. Figure 11(c) and (d) demonstrate that this initial improved mixing appears confined to only the radial locations within the duct inner diameter. The initial transient Z_{Bilger} behavior is a potential contributing factor for the decreased soot production observed in the DFI case.

The transient mixing behavior reported in Figure 11 is further illustrated in physical space through contours of the local equivalence ratio, ϕ, in Figure 12. ϕ is computed as the ratio between the local fuel mass and local O_2 mass, normalized by the stoichiometric fuel/O_2 ratio f_{st}. Starting with the leftmost panels at $t - \tau_{ign} = -0.05$ *ms* (just before ignition) we observe that the DFI case exhibits a larger spatial regime of ϕ values that are near stochiometric ($1 \lessapprox \phi \lessapprox 3$), compared with the corresponding free spray contour. These near-stoichiometric ϕ values are especially prevalent in the leading edge of the spray periphery. Just as in the Z_{Bilger} behavior at early times for Figure 11, we observe a larger prevalence of closer-to-stoichiometric mixture values in the DFI case, yielding the potential to produce less emissions via more complete combustion. In the rightmost panels at $t - \tau_{ign} = 0.50$ *ms*, we observe that the contours of ϕ between the DFI and free spray cases do not display significant differences in distribution or physical characteristics. This ϕ behavior for $t \gg \tau_{ign}$ is in agreement with the Z_{Bilger} behavior from Figure 11. Again, it appears to be the initial transient increase in fuel/air mixing that contributes toward the DFI case's decreased soot production.

Conclusions

In the current investigation, LES computations are performed for transcritical n-dodecane spray injection in

order to investigate DFI as a concept to achieve increased combustion efficiency and soot attenuation. A diffuse-interface method is used with finite-rate chemistry and real-fluid thermodynamic and transport property considerations. Differences in behavior between the DFI and free spray cases are highlighted. For both, the ignition delay time and flame lift-off length show relative agreement with past studies. Soot results using the two-equation Moss-Brookes model confirms the decreased soot obtained in the DFI case, in agreement with previous findings. The results of the study serve as evidence that diffuse-interface methods can be used to capture diesel spray behavior under varying conditions and geometries and help to achieve better understanding of the complex fluid, mixing and chemical processes.

The region inside the duct exhibited an environment of low pressure, which had been a point of disagreement in the literature, that caused a jet-pump effect and increased the velocity magnitude in the DFI case. This increased air entrainment was shown to (i) increase the kinetic energy, which potentially improves the turbulent mixing, and (ii) reduce the global equivalence ratio inside the duct. The closer-to-stoichiometric mixture observed in the DFI case was further demonstrated by analyzing probability distributions of the mixture fraction and by observing contours of the local equivalence ratio, which specifically highlighted the improved initial transient mixing. This change in mixture composition is likely to be a contributing factor to reducing the opportunity to form incomplete combustion products and soot.

Two analytical modeling strategies were applied to estimate the entrained air inside the duct. The first one, based on Bernoulli's principles, highlighted the relation between the decreased pressure and increased mass flow inside the duct. The second one, rooted in the literature of ejectors, did not require a priori knowledge of the pressure drop caused by the duct, and predicted reasonably well the mass flow rate of the entrained air. While further work is needed to assess the validity and relevance of these formulations, these models could help to design and analyze DFI configurations.

Declaration of conflicting interests

The author(s) declared no potential conflicts of interest with respect to the research, authorship, and/or publication of this article.

ORCID iDs

Jack Guo https://orcid.org/0000-0003-4090-9289
Wai Tong Chung https://orcid.org/0000-0002-6447-4008
Matthias Ihme https://orcid.org/0000-0002-4158-7050

References

1. Chambers M and Schmitt RR. Diesel-powered passenger cars and light trucks. *Bureau of Transportation Statistics*, https://www.bts.gov/archive/publications/bts_fact_sheets/oct_2015/entire (2015, accessed 31 October 2022).
2. O'Connor J and Musculus M. Post injections for soot reduction in diesel engines: a review of current understanding. *SAE Int J Engines* 2013; 6(1): 400–421.
3. Upatnieks A, Mueller CJ and Martin GC. The influence of charge-gas dilution and temperature on DI diesel combustion processes using a short-ignition-delay, oxygenated fuel. SAE technical paper 2005-01-2088, 2005.
4. Mueller CJ, Nilsen CW, Ruth DJ, Gehmlich RK, Pickett LM and Skeen SA. Ducted fuel injection: A new approach for lowering soot emissions from direct-injection engines. *Appl Energy* 2017; 204: 206–220.
5. Bergmann M, Kirchner U, Vogt R and Benter T. On-road and laboratory investigation of low-level PM emissions of a modern diesel particulate filter equipped diesel passenger car. *Atmos Environ* 2009; 43(11): 1908–1916.
6. Johnson T and Joshi A. Review of vehicle engine efficiency and emissions. *SAE Int J Engines* 2018; 11(6): 1307–1330.
7. Dumitrescu CE, Cheng AS, Kurtz E and Mueller CJ. A comparison of methyl decanoate and tripropylene glycol monomethyl ether for soot-free combustion in an optical direct-injection diesel engine. *J Energy Resour Technol* 2017; 139(4): 042210–042211.
8. Polonowski CJ, Mueller CJ, Gehrke CR, et al. An experimental investigation of low-soot and soot-free combustion strategies in a heavy-duty, single-cylinder, direct-injection, optical diesel engine. SAE technical paper 2011-01-1812, 2011.
9. Fitzgerald RP, Svensson K, Martin G, Qi Y and Koci C. Early investigation of ducted fuel injection for reducing soot in mixing-controlled diesel flames. *SAE Int J Engines* 2018; 11(6): 817–833.
10. Liu X, Mohan B and Im HG. Numerical investigation of the free and ducted fuel injections under compression ignition conditions. *Energy Fuels* 2020; 34(11): 14832–14842.
11. Zhang Y, Wang Z, Lee CF, Li F and Wu H. Analysis of mechanism of ducted fuel injection under non-vaporizing condition. *Fuel* 2021; 305: 121496.
12. Ong JC, Zhang M, Jensen MS and Walther JH. Large eddy simulation of soot formation in a ducted fuel injection configuration. *Fuel* 2022; 313: 122735.
13. Millo F, Piano A, Peiretti Paradisi B, et al. Ducted fuel injection: Experimental and numerical investigation on fuel spray characteristics, air/fuel mixing and soot mitigation potential. *Fuel* 2021; 289: 119835.

14. Nilsen CW, Yraguen BF, Mueller CJ, Genzale C and Delplanque JP. Ducted fuel injection vs. Free-spray injection: A study of mixing and entrainment effects using numerical modeling. *SAE Int J Engines* 2020; 13(5): 705–716.

15. Gehmlich RK, Mueller CJ, Ruth DJ, Nilsen CW, Skeen SA and Manin J. Using ducted fuel injection to attenuate or prevent soot formation in mixing-controlled combustion strategies for engine applications. *Appl Energy* 2018; 226: 1169–1186.

16. Nilsen CW, Biles DE and Mueller CJ. Using ducted fuel injection to attenuate soot formation in a mixing-controlled compression ignition engine. *SAE Int J Engines* 2019; 12(3): 309–322.

17. Zhang M, Ong JC, Pang KM, Bai XS and Walther JH. An investigation on early evolution of soot in n-dodecane spray combustion using large eddy simulation. *Fuel* 2021; 293: 120072.

18. Ma PC, Lv Y and Ihme M. An entropy-stable hybrid scheme for simulations of transcritical real-fluid flows. *J Comput Phys* 2017; 340: 330–357.

19. Ma PC, Wu H, Jaravel T, Bravo L and Ihme M. Large-eddy simulations of transcritical injection and auto-ignition using diffuse-interface method and finite-rate chemistry. *Proc Combust Inst* 2019; 37(3): 3303–3310.

20. Ihme M, Ma PC and Bravo L. Large eddy simulations of diesel-fuel injection and auto-ignition at transcritical conditions. *Int J Engine Res* 2019; 20(1): 58–68.

21. Chung WT, Ma PC and Ihme M. Examination of diesel spray combustion in supercritical ambient fluid using large-eddy simulations. *Int J Engine Res* 2020; 21(1): 122–133.

22. Engine Combustion Network, Sandia National Laboratory, https://ecn.sandia.gov/ (2008, accessed 1 May 2022).

23. Chung TH, Ajlan M, Lee LL and Starling KE. Generalized multiparameter correlation for nonpolar and polar fluid transport properties. *Ind Eng Chem Res* 1988; 27(4): 671–679.

24. Takahashi SHINJI. Preparation of a generalized chart for the diffusion coefficients of gases at high pressures. *J Chem Eng Jpn* 1975; 7(6): 417–420.

25. Peng DY and Robinson DB. A new two-constant equation of state. *Ind Eng Chem Fundam* 1976; 15(1): 59–64.

26. Poling BE, Prausnitz JM and O'Connell JP. *Properties of gases and liquids*. New York, NY: McGraw-Hill, 2001.

27. Miller RS, Harstad KG and Bellan J. Direct numerical simulations of supercritical fluid mixing layers applied to heptane–nitrogen. *J Fluid Mech* 2001; 436: 1–39.

28. Congiunti A, Bruno C and Giacomazzi E. Supercritical combustion properties. In: *41st Aerospace sciences meeting and exhibit*, Reno, Nevada, 6–9 January 2003, AIAA paper 2003-478. Reston, VA: AIAA.

29. Hickey JP, Ma PC, Ihme M, et al. Large eddy simulation of shear coaxial rocket injector: real fluid effects. In *49th AIAA/ASME/SAE/ASEE Joint propulsion conference*, San Jose, CA, 14–17 July 2013, AIAA paper 2013-4071. Reston, VA: AIAA.

30. Ma PC, Bravo L and Ihme M. Supercritical and transcritical real-fluid mixing in diesel engine applications. In: *Proceedings of the summer program*, 2014, pp.99–108. Center for Turbulence Research, Stanford University.

31. Brookes S and Moss J. Predictions of soot and thermal radiation properties in confined turbulent jet diffusion flames. *Combust Flame* 1999; 116(4): 486–503.

32. Pang KM, Ng HK and Gan S. Simulation of temporal and spatial soot evolution in an automotive diesel engine using the moss–Brookes soot model. *Energy Convers Manag* 2012; 58: 171–184.

33. Zhang X, Wang N, Xie Q, Zhou H and Ren Z. Global sensitivity analysis and uncertainty quantification of soot formation in an n-dodecane spray flame. *Fuel* 2022; 320: 123855.

34. Watanabe H, Kurose R, Komori S and Pitsch H. Effects of radiation on spray flame characteristics and soot formation. *Combust Flame* 2008; 152(1-2): 2–13.

35. Khalighi Y, Nichols JW, Lele SK, et al. Unstructured large eddy simulation for prediction of noise issued from turbulent jets in various configurations. In: *17th AIAA/CEAS aeroacoustics conference (32nd AIAA aeroacoustics conference)*, Portland, OR, 5–8 June 2011, AIAA paper 2011-2886. Reston, VA: AIAA.

36. Strang G. On the construction and comparison of difference schemes. *SIAM J Numer Anal* 1968; 5(3): 506–517.

37. Wu H, Ma PC and Ihme M. Efficient time-stepping techniques for simulating turbulent reactive flows with stiff chemistry. *Comput Phys Commun* 2019; 243: 81–96.

38. Gottlieb S, Shu CW and Tadmor E. Strong stability-preserving high-order time discretization methods. *SIAM Rev* 2001; 43(1): 89–112.

39. Vreman AW. An eddy-viscosity subgrid-scale model for turbulent shear flow: algebraic theory and applications. *Phys Fluids* 2004; 16(10): 3670–3681.

40. Colin O, Ducros F, Veynante D and Poinsot T. A thickened flame model for large eddy simulations of turbulent premixed combustion. *Phys Fluids* 2000; 12(7): 1843–1863.

41. Pickett L, Bruneaux G and Payri R. Engine combustion network special issue. *Int J Engine Res* 2020; 21(1): 11–14.

42. Malbec LM, Egúsquiza J, Bruneaux G and Meijer M. Characterization of a set of ECN spray A injectors: nozzle to nozzle variations and effect on spray characteristics. *SAE Int J Engines* 2013; 6(3): 1642–1660.

43. Watanabe N, Kurimoto N, Serizawa K, Yoshino M, Skeen S and Pickett LM. Identification of significant design factors for diesel spray combustion control through comprehensive experiments with various multi-hole nozzle internal geometries. *Int J Engine Res* 2022; 23(2): 319–333.

44. Lillo PM, Pickett LM, Persson H, Andersson O and Kook S. Diesel spray ignition detection and spatial/temporal correction. *SAE Int J Engines* 2012; 5(3): 1330–1346.

45. Wehrfritz A, Kaario O, Vuorinen V and Somers B. Large eddy simulation of n-dodecane spray flames using flamelet generated manifolds. *Combust Flame* 2016; 167: 113–131.

46. Westlye FR, Battistoni M, Skeen SA, et al. Penetration and combustion characterization of cavitating and non-cavitating fuel injectors under diesel engine conditions. SAE technical paper 2005-01-2088, 2005.

47. Bilger RW. The structure of diffusion flames. *Combust Sci Technol* 1976; 13: 155–170.

48. Li F, Lee CF, Wang Z, Pei Y and Lu G. Impacts of duct inner diameter and standoff distance on macroscopic spray characteristics of ducted fuel injection under non-vaporizing conditions. *Int J Eng Res* 2021; 22(5): 1702–1713.

49. Koukouvinis P, Vidal-Roncero A, Rodriguez C, Gavaises M and Pickett L. High pressure/high temperature multiphase simulations of dodecane injection to nitrogen: application on ECN Spray-A. *Fuel* 2020; 275: 117871.

50. Maes N, Meijer M, Dam N, et al. Characterization of spray A flame structure for parametric variations in ECN constant-volume vessels using chemiluminescence and laser-induced fluorescence. *Combust Flame* 2016; 174: 138–151.

51. Skeen SA, Manin J, Pickett LM, et al. A progress review on soot experiments and modeling in the engine combustion network (ECN). *SAE Int J Engines* 2016; 9(2): 883–898.

52. Pei Y, Som S, Pomraning E, et al. Large eddy simulation of a reacting spray flame with multiple realizations under compression ignition engine conditions. *Combust Flame* 2015; 162(12): 4442–4455.

53. Pang KM, Jangi M, Bai XS, Schramm J, Walther JH and Glarborg P. Effects of ambient pressure on ignition and flame characteristics in diesel spray combustion. *Fuel* 2019; 237: 676–685.

54. Pritchard R, Guy JJ and Connor NE. *Industrial gas utilization*. New Providence, NJ: Bowker, 1977.

55. Singh G, Sundararajan T and Shet USP. Entrainment and mixing studies for a variable density confined jet. *Numer Heat Transf A Appl* 1999; 35: 205–224.

56. Kolluri P, Kamal A and Gollahalli SR. Application of noncircular primary-air inlet geometries in the inshot burners of residential gas furnaces. *J Energy Resour Technol* 1996; 118: 58–64.